Frontiers | Frontiers in Sustainability

TYPE Mini Review
PUBLISHED 31 August 2022
DOI 10.3389/frsus.2022.926438

EDITED BY
Rajib Mukherjee,
Texas A&M University, United States

REVIEWED BY
Adrian Loy,
Monash University, Australia

*CORRESPONDENCE
Paola Rodriguez-Estupiñán
jp.rodrigueze@uniandes.edu.co

SPECIALTY SECTION
This article was submitted to Sustainable Chemical Process Design, a section of the journal Frontiers in Sustainability

RECEIVED 22 April 2022
ACCEPTED 18 July 2022
PUBLISHED 31 August 2022

CITATION
Hernández-Barreto DF, Bernal V, Giraldo L, Moreno-Piraján JC and Rodriguez-Estupiñán P (2022) Biomass valorization by thermal treatments: Graphene-based materials and their application on glyphosate adsorption. *Front. Sustain.* 3:926438.
doi: 10.3389/frsus.2022.926438

Biomass valorization by thermal treatments: Graphene-based materials and their application on glyphosate adsorption

Diego Felipe Hernández-Barreto[1], Valentina Bernal[1], Liliana Giraldo[2], Juan Carlos Moreno-Piraján[1] and Paola Rodriguez-Estupiñán[1]*

[1]Grupo de Investigación de Sólidos Porosos y Calorimetría, Departamento de Química, Universidad de los Andes, Bogotá, Colombia, [2]Grupo de Investigación de Calorimetría, Departamento de Química, Universidad Nacional de Colombia, Bogotá, Colombia

Carbon-based nanomaterials have exceptional physicochemical properties like high surface area and active sites, suitable for the adsorption of inorganic and organic compounds. Currently, these materials are being tested for environmental applications, e.g., detecting emerging pollutants in drinking and surface water. This work reviews different methods to prepare graphene (G) or graphene-based materials (GBM) using biomass or its constituents. This text brings together the methods used to revalue biomass by converting it into graphene materials from thermal treatments and their application in the adsorption of glyphosate from an aqueous solution. Computational studies were also added to evaluate the information about interactions between the herbicide and graphene layers.

KEYWORDS

pyrolysis, graphene, glyphosate, adsorption, biomass waste

Introduction

Graphene (G) and graphene-based materials (GBMs) have been exceptional compounds due to their superior mechanical, electronic, thermal, and optical properties. These characteristics make them suitable materials for adsorption, photocatalysis, energy storage, gas sensing, and medical applications (Aïssa et al., 2015). However, the disadvantages of these materials are the high cost of scaling up the process and the environmental impact of some of the production methods; for this reason, it is important to develop greener alternatives for G and GBM production. Several methodologies for the synthesis of G have been reported in the literature, and are classified as top-down and bottom-up approaches. Graphite oxidation-exfoliation is the most usual top-down method (Kumar et al., 2021), while chemical vapor deposition (CVD) is the most common bottom-up method (Saeed et al., 2020). Both methods have advantages like high-quality material obtention and disadvantages like limited G quantities, low cost-effective processes, and high environmental impact.

To achieve a higher cost-effective process, higher G yield, and reduce the environmental impact, G synthesis using monomers and biopolymers (Li et al., 2016) (bottom–up methods) or precursors with high carbon content like biomass wastes (Purkait et al., 2017) (top-down methods) and thermochemical treatments like pyrolysis have been developed. In countries like Canada, the biomass waste from agriculture is close to 82.4 million tons, of which 27 million tons was used to manufacture bioproducts generating $1.3 billion (Antar et al., 2021). The circular economy is promoted using this type of precursor by valorizing wastes and decreasing the economic cost and environmental damage (Sillanpä and Ncibi, 2019).

Graphene is a hexagonal monolayer formed by sp^2 hybridized carbon atoms, but some defects can appear during the synthesis. They are classified as intrinsic when the crystalline order is modified without the presence of foreign atoms (vacancies, 5 or 7 carbon rings) or extrinsic if G has impurities in the lattice (N, O, and Si). These atoms can extend to a more carbonaceous network, and the reduced dimensionality of G is related to a lower number of possible defect types (Banhart et al., 2010). On the other hand, some authors consider that the G synthesis by top-down methods decreases the possibility of obtaining G with defects. This finding is important because they can affect the performance of G in some applications, such as electronic and optic applications (Liu et al., 2015). Figure 1 shows the pristine G and G with intrinsic and extrinsic defects.

Lignocellulosic biomass comprises five primary components: cellulose, hemicellulose, lignin (between the three constitute 85–90%), volatiles, and ash. Cellulose is the most abundant biopolymer on the earth and is formed by glucose. Hemicellulose and lignin are heteropolymers constituted by polysaccharides and polyalcohols, respectively (Ding et al., 2021).

Two methods have been used for the synthesis of G from biomass. The first increases the amount of fixed carbon in the biomass by subjecting it to pyrolysis or torrefaction. Later, the product produced by this process is combined with metallic salts, and a heat treatment is carried out at high temperatures. In the other method, monomers of the macromolecules constituting the biomass are used; they are united through chemical reactions catalyzed by temperature, ultrasonic or ultraviolet radiations, and organic linkers. The G material obtained by the two methods is expected to have similar physicochemical properties. However, some interactions between char and the volatile compounds released during the direct pyrolysis of biomass can affect the result (Ding et al., 2021).

In part, G materials can be obtained from both methods because many chemical reactions can be carried out by increasing the temperature or adding catalysts, e.g., the Diels-Alder reaction. Kong et al. indicated that pyrolysis of biomass produced highly porous G, and hence processes at high temperatures (graphitization and activation) are used to prepare high surface area G compounds. However, the materials obtained can have disordered layers and defects. They are classified as graphene-like materials because, despite the imperfections, they show the physicochemical properties of G (Kong et al., 2020).

Many techniques can be applied to prepare graphene-like materials. Some include the salt-based method, template-based confinement, chemical blowing, coupling with hydrothermal treatment, and post-exfoliation (Kulyk et al., 2022). We will focus on the first two methods with particular emphasis on the salt-based methods because they are the most used techniques to prepare G from biomass. We emphasize that the samples obtained by pyrolytic methods, such as those presented below, will always require exfoliation after the heat treatment. However, the literature suggests several studies on this topic.

Understanding the relationship between biomass and graphene materials: How to increase the added value of some wastes?

Salt-based method

This method uses salts or mixtures that allow, among other things, to increase the surface area and porosity during the activation. The most common compounds contain potassium (KOH, K_2CO_3, and K_2O) because this cation can intercalate in the carbonaceous structure of the precursor, and the lattice increases during thermal treatment. Furthermore, potassium salts can participate in redox reactions, increasing the degassing (release of H_2O and CO_2) and, therefore, the porosity of the G-like material (Nanaji et al., 2021).

Materials with controlled physicochemical characteristics can be produced using different potassium salts. The impregnation of soybean shell with KOH generates graphene materials with a surface area of 1,152 m^2 g^{-1}; this result can be compared with materials obtained when the impregnation salt is potassium formate, whose surface area increases to 1,816 m^2 g^{-1}, and the mesopore volume also increases. Conversely, the layer thickness decreases (near to 3.8 nm), indicating that the G material comprises fewer layers, making it suitable for electronic and optical applications (Liu et al., 2022).

Sucrose is a glycosyl glycoside present in biomass, and it is formed by the combination of one molecule of glucose and one molecule of fructose. This compound was mixed with KOH in a ratio of 1:0.3 (sucrose: KOH) (Dorontić et al., 2021), and the mixture was dissolved in distilled water and subjected to hydrothermal treatment at 170°C for 4 h. When the autoclave was cooled, the product was dialyzed to remove any residue of sucrose. Thus, graphene quantum dots (GQD) doped with

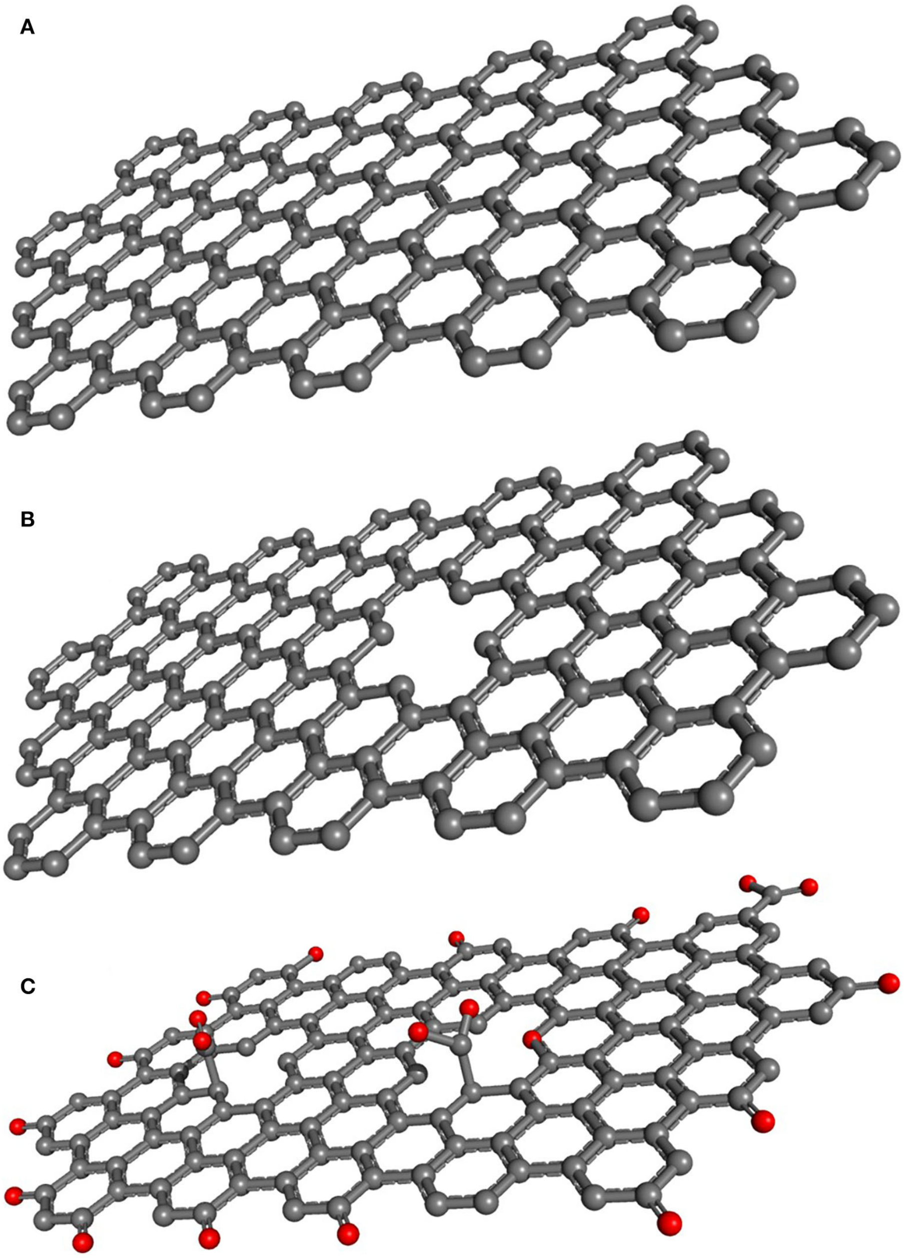

FIGURE 1
(A) Pristine graphene, **(B)** graphene with intrinsic defects, and **(C)** graphene with extrinsic defects.

potassium atoms were obtained. The authors indicate that the action mechanism involves cycloaddition/elimination pathways. The GQD have an average diameter of 3.4 nm, and the crystal structure was hexagonal similar to the undoped quantum dots. The main surface chemical groups on G materials produced using potassium salts are C=C, C–C, C–H, C–O–C, C–O–H, and C=O. For these chemical bonds, some authors report XPS peaks at 285.3 eV, 286.4 eV, 287.3 eV, 288.3 eV, 533.0 eV, and 531.7 eV respectively. The bands associated with oxygenated groups are significant because these groups facilitate the exfoliation of G layers in materials like graphite oxide. It avoids additional steps in the synthesis of G materials, like oxidation by the Hummers method (Dorontić et al., 2021).

Glucose was also used to produce G-like structures using potassium salts. The LiCl/KCl (molten salt: melting point of 353°C) mixture was investigated to prepare G materials composed of few-layer G. This salt is mixed with glucose in a ratio of 1:100 (Glucose: salt) and thermal treatment at 500–800°C. The carbon nanostructures are generated from glucose polymerization in a solvent reaction medium formed by the ionic species (salts) (Liu et al., 2014). The amorphous carbon was obtained with different pore sizes and high hydrophobicity. However, the process converts the glucose monomers to pure few-layer graphene at a low concentration of carbohydrates. According to the authors, dehydration begins at temperatures below 200°C (water elimination), and many intermediate products can react between them and generate carbonaceous matter or sp^2 C–C bonds. Wang et al. indicated that the chlorates from molten salt (LiCl/KCl) catalyze intermolecular and intramolecular dehydration reactions (Wang et al., 2016).

Experimentally, this finding is corroborated using X-ray diffraction (XRD) studies; the results showed a change in the peak position (2θ) from 18 to 23°, indicating a decrease in the C-C bond distance due to the release of water when the temperature increases. Raman spectroscopy also showed a rise in the I_G/I_D ratio and the peak formation at 2,600 cm^{-1} associated with the 2D peak and sp^2 carbon atoms (Liu et al., 2022).

On the other hand, at temperatures close to 300°C, caramelization reactions (Maillard reaction) prevent the salt from melting, forming a single phase where the product does not have the characteristics of G or its derivatives. Above this temperature (e.g., 700°C), two phases are observed by liquefaction of the salt. Moreover, the structure undergoes rearrangements, increasing the graphitic material by crystallization. In this regard, at low temperatures ($<$300°C), the surface area decreases from 630 (at 700°C) to 30 $m^2\ g^{-1}$ (Li et al., 2017).

Temperature is not the only factor that affects the surface area. Modifications in the methodology or precursor can also influence this parameter. A summary is shown in the following table.

Table 1 presents the data of GBMs with high surface area; this turns out to be a challenge because, generally, the graphitization processes entail a decrease in the parameter. Depending on the material application, the surface area could be crucial, e.g., the low surface area limits the power capacity in a supercapacitor and sensors, and this parameter plays a significant role in adsorption capacity.

Among the salt processes to prepare graphene materials, we found a method called simultaneous graphitization-activation (SAG). This process allows the synthesis of two-dimensional (2D) carbon-based materials with intermediate properties between graphene and porous materials (graphene-like nanosheets, PGNS). In addition to the advantages already mentioned, these materials present a reduction in environmental pollution compared to synthesizing graphene oxide (GO) through the Hummers method (Ambika and Srilekha, 2021).

The SAG method involves the incorporation of the graphitization ($FeCl_3$) and activation ($ZnCl_2$) agents simultaneously in the carbonaceous matrix (biomass). The chemical reactions are catalyzed by the temperature ($>$850°C, 1 h), and an inert atmosphere is necessary when the pyrolysis is carried out. Graphitization is catalyzed by Fe^{3+} ions of the carbon source, forming a carburized phase, and $ZnCl_2$ is used during activation to generate porous structures (Hou et al., 2015).

Template-based methods

This method uses templates on which the carbon source (biomass or its constituents) is deposited to form graphene sheets after heat treatment. Ruiz-Hitzky et al. used sucrose as a carbon source and sepiolite (a layered silicate) as inorganic support. They melted the sucrose on the support to form humin (polymeric material resulting from water loss and volatile organic species). The polymer intercalation in the silicate is assisted by microwave irradiation generating clay-humin nanocomposites. Then, this structure will form graphene-like-clay nanocomposites by thermal treatment at 750°C in an inert atmosphere. The XRD results obtained by the authors showed that the graphene-like-clay nanocomposites have an interlayer distance carbon-clay of 0.4 nm (Ruiz-Hitzky et al., 2011).

Electrochemical impedance spectroscopy (EIS) measurements corroborated the conversion of molten caramel to graphene. It is observed that the intercalation of the nanocomposite containing humin in the silicate increases the electrical conductivity from 10^{-12} S cm^{-1} (in the material generated after thermal treatment) to 10^{-1} S cm^{-1} (Ruiz-Hitzky et al., 2011).

Likewise, the presence of graphene is corroborated by ^{13}C NMR analysis, where a single band at 125 ppm is observed, indicating the formation of C=C bonds from aromatic groups. Additionally, no bands are associated with oxygenated groups, suggesting that GO was not formed (Ruiz-Hitzky et al., 2011).

The material previously described was used in electronic applications due to the decrease in the composite surface area to 1 $m^2\ g^{-1}$ by the humin incrustation in the clay porosity. The authors suggest using other laminated clays with higher porosity (Ruiz-Hitzky et al., 2011).

Tang et al. used carbohydrates (glucose, fructose, and sucrose) and PEG 20000 as carbon sources and soft template, respectively. The authors mixed 8.9 wt% glucose solutions and 0.2 wt% PEG solutions in glass bottles with a tightened cover; the bottle was heated in a conventional microwave oven at 595 W for 1, 3, 5, 7, or 9 min (microwave-assisted hydrothermal conditions). According to the authors, PEG 20000 forms micelles, in which sugars are incorporated using microwaves. Then, the mixture is cooled to room temperature. A color change

TABLE 1 Summary of conditions used to prepare G and GBM and their surface area.

Precursor	Conditions	Surface area (m^2 g^{-1})
Gingko shells (Hong et al., 2021)	Biomass, NaCl and Urea (0.5:1.4:4 g)	1,133
Cellulose (Perondi et al., 2021)	Cellulose, $FeCl_3$ and $ZnCl_2$ (30 g: 3M; $ZnCl_2$ ratio 1:3 biomass:salt) Pyrolysis temperature: 700°C	1,229
Cellulose (Perondi et al., 2021)	Cellulose, $FeCl_3$ and $ZnCl_2$ (30 g: 3M; $ZnCl_2$ ratio 1:6 biomass:salt) Pyrolysis temperature: 700°C	1,227
Coconut shell (Sun et al., 2013)	Coconut shell, $ZnCl_2$, $FeCl_3$ (3g:9g:50mL of 3M solution) Activation-graphitization conditions: N_2 atmosphere by heating the sample at 900°C for 1 h	1,874
Sorghum stalk (Khalil et al., 2017) (activated carbon with graphene-like structure)	Stalk:$ZnCl_2$ (15 g:200 mL of 10% solution) Pyrolysis: 500°C for 1h	1,817
Lignin (Ma et al., 2020) (Activated carbon with graphene-like structure)	Lignin:$ZnCl_2$ (1:2) Pyrolysis: 450°C for 2h	1,769

from transparent to light yellow corroborated the presence of GQD in the solution. Electron energy loss spectroscopy evaluated the structure and chemical composition of GQD. The results showed oxygenated surface groups (539 eV), but the main signals were found at 284 and 291 eV, peaks related to sp^2 C=C bonds (Tang et al., 2013).

In addition to clays, zeolites, and other laminar materials, compounds such as boric acid can be used as a template. Ling et al. used boric acid dissolved in distilled water and mixed it with gelatin (other proteins from biomass could be used) in a 10:1 ratio. The solution was stirred at 80°C until the water had evaporated entirely. The obtained material consists of boric acid nanoplates coated by a gelatin layer (thin thickness of 100–200 nm). Finally, the composite was treated at 900°C for 1 h (ramp rate: 5°C min^{-1}) under an inert atmosphere. The sample was washed using reflux and centrifugation with deionized water for 1.5 h, followed by freeze-drying (Ling et al., 2016). After the heat treatment, carbon sheets and boron oxide were produced; the latter was removed with the washings, regenerating the initial boric acid. The carbon sheets obtained have a thickness of 5–8 nm (similar to G materials with 10–20 layers) and a surface area of 416 m^2 g^{-1}. Raman spectroscopy was also performed on the material; the intensity ratio I_D/I_G was around 1.27, indicating that the nanosheets exhibited a disordered structure (Ling et al., 2016).

Thermal methods to synthesize graphene conventional structures

Among the graphene preparation systems that include conventional thermal treatments, several can be mentioned and are described in the specialized literature. Several techniques have been established for graphene synthesis. However, mechanical cleavage (exfoliation) (Novoselov et al., 2004), chemical exfoliation (Viculis et al., 2003; Allen et al., 2010), chemical synthesis (Park and Ruoff, 2009), and chemical vapor deposition (CVD) synthesis (Reina et al., 2009) are the most commonly used methods at present. Other techniques, such as nanotube exfoliation (Jiao et al., 2009, 2010; Kosynkin et al., 2009) and microwave synthesis (Xin et al., 2010), have also been reported. Although mechanical exfoliation using an AFM cantilever allows the fabrication of few-layer graphene, the limitation of the process is that the thickness of graphene varies by ∼10 nm, which is comparable to 30-layer graphene.

Thermal methods to synthesize graphene advanced structures

Systems that can be classified as advanced systems for graphene synthesis are widely reported and are experimentally complex in terms of the setups and the experience that the experimenter must have. An interesting experiment has recently been published and is reported to be a very good example of this type of synthesis. The arc discharge system is constructed with an anode and a cathode graphite rod, which are attached to the mechanical feed channel; the anode was thus adjusted to the separation of the cathode. Both electrodes were allowed to hang inside a horizontal quartz tube, and the quartz tube was surrounded by a tungsten heating coil. They then placed inside the quartz tube and against the inner wall of the quartz tube a 0.2 2 cm, 50 mm thick Cu foil with a purity of 99.95%. The quartz tube with the vacuum arc electrodes was enclosed in a high vacuum chamber which was evacuated at a base pressure of 10^{-7} torr. The center of the quartz furnace was heated to various processing temperatures from 300 to 400°C. Next, a gaseous mixture of H_2 (10%) with Ar was introduced into the chamber for 120 min, and the furnace was heated to 600°C for 40 min and then held for 20 min under an ambient pressure of

50 torr. The H_2 contained at 600°C is essential for graphene growth. This pre-deposition process removed the native oxide and resurfaced the Cu surface to aid carbon diffusion and segregation. Next, the authors quenched H_2 and provided 40 V DC and 100 A electrical power through the vacuum gap of the graphite electrodes to cause a vacuum arc for 25 s. This generated a very high temperature of 2,400°C, vaporized the graphite, and injected carbon into the Cu surface. It also generated a very high flux of photons with a broad spectrum. By photon radiation, the Cu surface can be heated to its melting point within 1 s. After striking an arc under vacuum, the chamber was cooled down to the ambient temperature.

Characterize the graphene materials using NMR, FTIR, Raman, and PXRD

When synthesizing graphites, graphite oxides, and families of these compounds, it is important to perform an excellent characterization. One of the techniques to be used in this sense is to take Fourier-transform infrared (FTIR) spectra of the samples with a good number of scans using a suitable instrument; they are usually scanned between 4,000 and 600 cm^{-1}. Another important technique in graphene characterization is solid-state 13C nuclear magnetic resonance (NMR) spectra taken at a slew rate of 62.5 kHz (4.0 μs, 115 W). The X-ray photoelectron spectroscopy (XPS) analysis spectroscopy should be performed using an instrument equipped with a monochromatic Al Kα excitation source operating at 1,486.7 eV. X-ray diffraction patterns (PXRD) should be acquired using an instrument equipped with a $CuK_{\alpha 1/2}$ radiation source ($\lambda K_{\alpha} = 0.15406$ nm) and a Lynxeye type detector. Samples should be scanned in the 2θ range of 10–90° 2θ using a step size of 0.026 °. Raman and solid-state photoluminescence (PL) spectroscopy spectra can be obtained by having equipment with a dual-frequency Lexel SHG argon ion laser. Silica should be used as a substrate. Raman measurements were performed with a 514.5 nm laser (green), and PL measurements were performed with an excitation wavelength of 244 nm. Total scattering data were collected at the Brockhouse high energy beamline at the Canadian Light Source using a wavelength of $\lambda = 0.2081°$ and a PerkinElmer XRD1621 area detector XRD1621 positioned 160 mm downstream of the sample (Mokoloko et al., 2021).

Finally, an NMR is taken in the specific case of hydroxyapatite, which is reviewed in the literature. In this way, the solid state allows to analyze the evolution of the functional groups in the rGO-HAP *nanocomposite* (Rajesh et al., 2019). The 1 H and 31P NMR experiments were performed at room temperature using a 9.4 T Bruker magnet with a resonance frequency of 400.23 and 162.01 MHz, respectively. The 1 H and 31P chemical shifts were referenced using D2O [resonance at 4.79 parts per million (ppm)] and Li_3PO_4 (resonance at 10.3 ppm), respectively. Cross-polarized magic angle spinning (CPMAS) experiments were performed with a contact time of 5 ms. To obtain a complete picture of the effect of PAH NRs within rGO films, a commercial SPM (NTEGRA, NT-MDT) in CAFM and PFM modes was used to visualize the spatial distribution of the nanoscale sp^2 and sp^3 chemical environment around nanoHAP in rGO films, as well as to visualize their local piezoelectric behavior. For these measurements, samples dispersed in isopropanol were spin-coated on an n-type Si (1 0 0) substrate and dried at 40°C. CAFM and PFM measurements were performed using a Pt/Ir coated Si cantilever with a force constant and radius of curvature of ~2.8 Nm^{-1} and ~25 nm, respectively. The nanoscale displacement of the sample resulting from the application of an external ac field between a tip and the sample can be measured by PFM. In PFM measurements initially, samples are excited with a driving voltage $V = \mathrm{VDC} + \mathrm{VAC}\cos(\omega t)$ in the perpendicular direction, where VDC is the applied DC current bias and ω is the angular frequency of Vac. The voltage-dependent piezoelectric response of different regions of the rGO-HAP nanocomposite was imaged at various bias voltages (−2.5 to +2.5 V).

Overcoming graphene limitations in environmental applications: Adsorption of glyphosate herbicide using GBM nanocomposites

The application of G and GBM on glyphosate (GLY) adsorption has been studied in some investigations, including experimental and computational research. In this section, we will show and discuss the most relevant results of some investigations related to this application, compare them, and analyze the interactions and mechanisms involved in this type of process. We clarify that the materials presented here are GBM nanocomposites that can be used to improve graphene physicochemical characteristics and its performance in environmental applications.

Currently, there is an environmental and health concern over the use of herbicides. These are chemical agents that act in different metabolic pathways of undesirable plants, herbs, and weeds; due to the constant increase in worldwide food demand, massive use of these chemicals in agriculture has become necessary. Among others, glyphosate is one of the most controversial broad-spectrum herbicides that are currently used, although about 20 countries have banned it. The health and environmental risk of GLY is related to the induction of antibiotic resistance; toxicity in organisms like amphibians, fishes, and reptiles; endocrine disruption; metabolic alteration; and potential teratogenic, tumorigenic, and carcinogenic effects (Meftaul et al., 2020). Indeed, in 2015, the IARC classified GLY as a possible carcinogen (Group 2A) (International Agency for

Research on Cancer, 2015), and for this reason, it is relevant to study appropriate ways to remove this pollutant from the environment using technologies like adsorption.

Adsorption is the process that takes place when a solid is in contact with a fluid (gas or liquid). It consists of the adhesion of fluid molecules (adsorptive) on the solid surface (adsorbent), thus increasing the fluid density in the vicinity of an interface (adsorbate) (Rouquerol et al., 2014). This technique is widely used in water depuration, and it is crucial to study and understand the adsorption equilibrium, with the purpose of designing optimal adsorption systems. Adsorption is described by means of the adsorption isotherms, in which the Langmuir isotherm is the most popular model applied in aqueous media. In general, Langmuir's theory states that rates of adsorption and desorption should be equal, when adsorption equilibrium is achieved. This is a semiempirical model that assumes that adsorption takes place in definite homogeneous active sites (local and equivalent), creating an adsorbed layer of one molecule thick, which is known as a monolayer (Al-Ghouti and Da'ana, 2020). The equation that describes Langmuir isotherm in the aqueous phase is presented in the following equation:

$$q_e = \frac{q_m^* K_L^* C_e}{1 + K_L^* C_e}$$

where q_e is the adsorbed quantity at equilibrium per gram of adsorbent (mg g^{-1}), q_m is the maximum adsorption capacity per gram of adsorbent (mg g^{-1}), K_L is the Langmuir constant, related to the affinity of the binding sites (L mg^{-1}), and C_e is the concentration of adsorptive at equilibrium in the solution (mg L^{-1}). Adsorption depends on many factors (pH, ionic strength, adsorbent dose, temperature, etc.) that a single model cannot describe it totally. However, Langmuir's approach describes very well most of the adsorption systems in aqueous solution, and for that reason, q_m is an acceptable parameter to compare and analyze adsorption of GLY by different GBM nanocomposites.

As mentioned, adsorption is an interface process, so it is important to understand the nature of the adsorbate–adsorbent interactions. To do so, it is necessary to analyze the physicochemical characteristics of GLY and GBM. First, GLY, also named as N-(phosphonomethyl) glycine (IUPAC), is a relatively small organic molecule that contains a carboxyl moiety ($-CO_2H$), amino moiety (–NH), and phosphonic acid moiety [$-PO(OH_2)$], which can undergo protonation and deprotonation reactions according to the pKa values. Thus, when GLY is dissolved in water, it can be found as a cationic, anionic, or zwitterionic form, depending on the degree of protonation of each functional group, i.e., depending on the pH of the solution. In addition, GLY has an amphoteric nature due to the presence of a basic group (amine) and two acidic groups (carboxylic and phosphonate) in its structure.

On the other hand, as mentioned earlier, G is a single-atom-thick material with a honeycomb lattice of sp^2 hybridized carbon atoms, and therefore, it presents local aromaticity with two π-electrons distributed over every hexagonal ring (Figure1A). For this reason, G could interact *via* π–π interactions with aromatic molecules or *via* π–cation or π–anion interactions with charged molecules and atoms. The lack of surface functional groups impedes other types of interactions with molecules like GLY. As it does not possess an aromatic ring, the interaction between GLY and G is restricted to π–anion or π–cation interactions, besides van der Waals interaction (forces). In addition, as G is a nano-sized material, its recovery or separation from solution is toilsome, and it hinders the possibility to use this material in fixed-bed column adsorption (dynamic adsorption). Consequently, new G derivatives have been designed and developed to overcome these disadvantages, thus increasing its capacity to interact with GLY and facilitating its recovery after adsorption is completed.

Novel GBM have been synthesized for application in glyphosate adsorption, including metal-doped graphene, magnetic reduced graphene oxide (rGO), MOF-G composites, and graphene aerogels, among others. As shown previously, the materials obtained *via* the thermal treatment of biomass differ from pristine G, because they present impurities, defects, and surface functional groups, such as epoxy, carbonyl, carboxyl, hydroxyl, anhydride, phenolic, lactone, and quinone, and it could be doped with heteroatoms to produce GO, rGO, and doped G. In general, these characteristics avoid the use of Hummers method to obtain GO, which has been used in all the cited articles.

Magnetic composites draw the attention of investigators because they present several advantages like ease of separating from solution (using a magnet), the presence of metallic centers that create new active adsorption sites, and an increase in particle size. In 2016, researchers of Université Laval reported the first study related to GLY adsorption onto magnetic GBM (Ueda Yamaguchi et al., 2016). They synthesized reduced graphene oxide (rGO) decorated with manganese ferrite nanoparticles ($MnFe_2O_4$-rGO) using a one-pot solvothermal method. The obtained composite has a morphology characterized by fully uniformly anchored microspheres (∼350 nm) composed of $MnFe_2O_4$ nanoparticles (∼15 nm) distributed over the rGO surface.

A complementary investigation was done in 2019 by researchers of the same university (Marin et al., 2019), who supported this composite ($MnFe_2O_4$-rGO) on vegetable-activated carbon ($MnFe_2O_4$-rGO/VAC) using an impregnation-evaporation method. $MnFe_2O_4$-rGO/VAC was synthesized as an alternative to increase granulometry of $MnFe_2O_4$-rGO and enable its application in fixed-bed column adsorption, and for this reason, batch adsorption of GLY was performed using $MnFe_2O_4$-rGO, while dynamic adsorption was carried out for $MnFe_2O_4$-rGO/VAC.

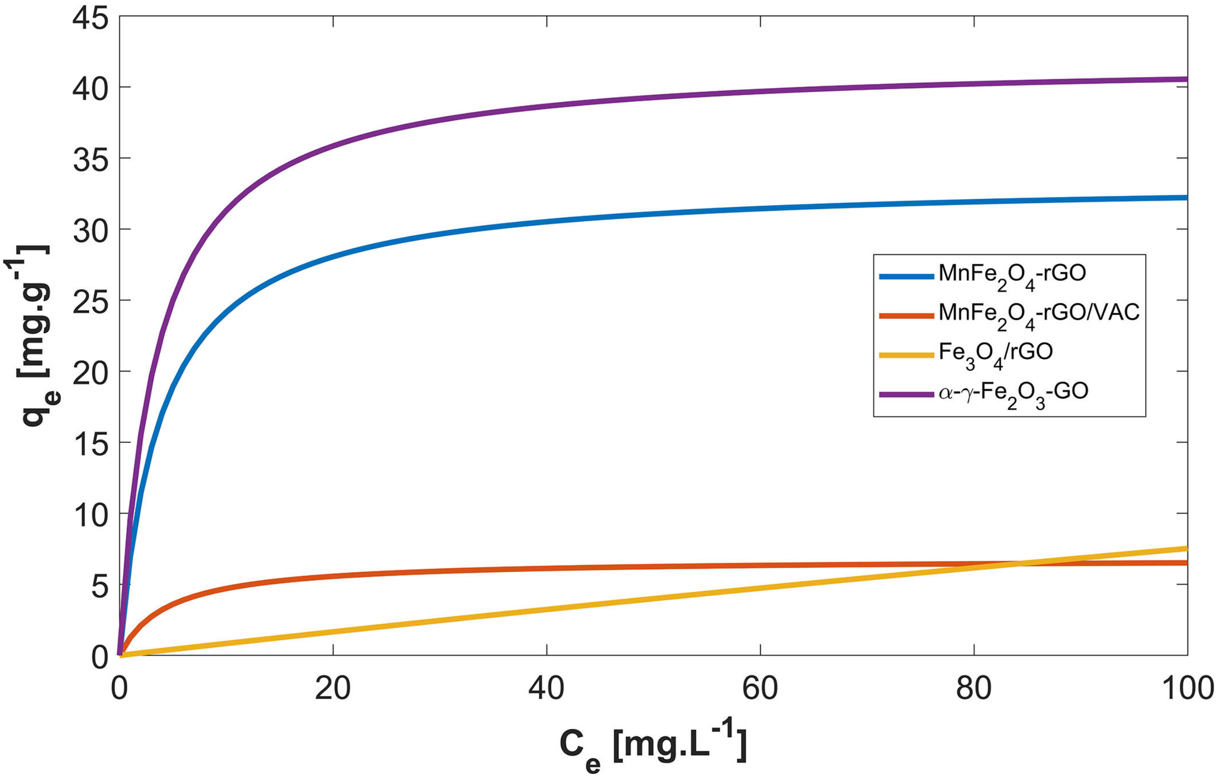

FIGURE 2
Simulated Langmuir isotherms using the parameters K_L and q_m calculated by the cited authors (Ueda Yamaguchi et al., 2016; Li et al., 2018; Marin et al., 2019; Santos et al., 2019).

Other examples of magnetic GBM composites are as follows. First, a nanocomposite of magnetite and rGO, labeled as Fe_3O_4/rGO, was synthesized through a coprecipitation method (Li et al., 2018). The authors obtained a composite with a rough surface characterized by the presence of Fe_3O_4 nanoparticles of different sizes over the rGO surface. Second, an adsorbent composed of GO functionalized with hematite and maghemite (α-γ-Fe_2O_3-GO) (Santos et al., 2019) was obtained by ultrasonication using propanol as solvent. This composite exhibited an average particle size of 50 nm, with quasi-cubic morphology, in which α-γ-Fe_2O_3 nanoparticles were well distributed over the GO surface.

All these composites have in common the use of iron oxides, besides GO and rGO. However, they were synthesized by different methods, different reactants, and different conditions that led to the production of different products. Indeed, these are composites of manganese ferrite ($MnFe_2O_4$), magnetite (Fe_3O_4), and iron oxide (III) (α-γ-Fe_2O_3). In general, they differ with respect to the oxidation state of iron, its crystal structure, and morphology, which attributes to the differences in their physicochemical properties. For example, in $MnFe_2O_4$, the oxidation states of iron and manganese are 3+ and 2+, respectively, with a spinel structure (cubic closed packed). Fe_3O_4 is also a ferrite, and in fact is the most common in nature. In this case, iron is presented as iron (II) and iron (III), in a spinel structure too. Finally, the oxidation state of iron in hematite and maghemite is 3+, but their crystal structures are hexagonal and cubic, respectively.

The adsorption results obtained by these composites are presented in Figure 2. Here, it is possible to observe the simulated Langmuir isotherms according to the parameters (K_L and q_m) calculated in each one of the articles at 25°C and using 1 $g.L^{-1}$ of adsorbent dose. It is interesting to compare them graphically to understand clearly how each parameter of the isotherm affects its behavior. First, the maximum adsorption capacity q_m is related to the plateau that appears when all the active sites are occupied by adsorbate molecules, i.e., no more molecules are adsorbed when concentration is raised. The higher the q_m value, the higher the plateau. Meanwhile, the Langmuir constant K_L is associated with the adsorbent–adsorbate affinity, so it is related to the pronunciation of the knee in the Langmuir plot. It means that when the initial slope of the isotherm is higher, the graph is closer to the *y*-axis; when the adsorbent–adsorbate affinity is higher than when the initial slope is smaller, the graph is farther to the *y*-axis. In conclusion, the higher the Langmuir constant $K_{L,}$ the higher the adsorbate–adsorbent affinity.

As can be seen in Figure 2, α-γ-Fe_2O_3-GO has the highest plateau, so it is expected to have the highest GLY adsorption capacity. However, the q_m value of Fe_3O_4/rGO is reported to be 65.4 mg.g^{-1}, almost 50% higher than the value of α-γ-Fe_2O_3-GO (q_m = 41.9 mg.g^{-1}). On the other hand, the composite $MnFe_2O_4$-rGO/VAC presented the lowest q_m value (6.8 mg g^{-1}), being ∼10 times smaller than Fe_3O_4/rGO and 5 times smaller than its homolog $MnFe_2O_4$-rGO (q_m = 33.4 mg g^{-1}). The unexpected behavior of the simulated isotherms can be attributed to its q_m value, which is due to the magnitude of the Langmuir constant K_L. Even though Fe_3O_4/rGO has the highest maximum adsorption capacity, it presents the lowest value of K_L (0.0013 L mg^{-1}). This finding indicates that the adsorbate–adsorbent affinity in this adsorption system is not adequate. Conversely, K_L values of $MnFe_2O_4$-rGO, $MnFe_2O_4$-rGO/VAC, and α-γ-Fe_2O_3-GO are 0.26, 0.22, and 0.29 L mg^{-1}, respectively, which is almost 100 times higher than the value of Fe_3O_4/rGO. This pattern is observed in the behavior of isotherms because Fe_3O_4/rGO curve is farther to the y-axis in comparison to the other isotherms. This shows the importance of obtaining not only maximum adsorption capacities but also great values of the Langmuir constant, because having a high adsorption capacity does not guarantee a high adsorbate–adsorbent affinity.

To understand the reason behind these differences, it is necessary to compare some physicochemical parameters, such as surface functional groups, surface area, and porosity. The FTIR spectra of all composites showed the typical surface groups of GO and rGO, like hydroxyl (∼3,400 cm^{-1}), carbonyl (∼1,650 cm^{-1}), aromatic carbon (∼1,150 cm^{-1}), and epoxy group (∼1,050 cm^{-1}). In addition, the vibrations due to Fe–O bond appear as two bands at 450 and 565 cm^{-1} for all composites, due to the presence of the magnetic iron oxide. Another important characteristic related to the surface functional groups is the surface charge, which is measured as the pH of the point of zero charge (pH_{PZC}) or isoelectric point (pH_{IEP}). This parameter describes the surface charge depending on the pH of the work solution. When pH > $pH_{PZC}/pH_{IEP,}$ the surface has a negative net charge; in contrast, when pH < $pH_{PZC}/pH_{IEP,}$ the surface net charge is positive. In this case, all composites have an acidic pH_{PZC}/pH_{IEP}. It is worth noting that all researchers assured that adsorption experiments were carried out in a solution with a pH < pH_{PZC}/pH_{IEP}, and hence the surface net charge of the composites was positive. In addition, considering the pKa values of GLY and the investigated pH values in each investigation (3.0–6.0), GLY has a net negative charge under these conditions. Therefore, electrostatic attraction forces between the positively charged surface of composites and negatively charged GLY are responsible for the adsorption.

With regard to textural parameters, the BET surface area trend is $MnFe_2O_4$-rGO >> α-γ-Fe_2O_3-GO = $MnFe_2O_4$-rGO/VAC, and unfortunately, no textural parameters were determined for Fe_3O_4/rGO. BET area of $MnFe_2O_4$-rGO (305 m^2 g^{-1}) is ∼15 times higher than the other two composites (20 m^2 g^{-1}). The average pore diameter of $MnFe_2O_4$-rGO, α-γ-Fe_2O_3-GO, and $MnFe_2O_4$-rGO/VAC is 3.4, 18, and 3.8 nm, respectively, since all of them are classified as mesoporous materials. Interestingly, α-γ-Fe_2O_3-GO does not have the highest surface area, although it has the highest adsorption capacity. So, it could be attributed to a better interaction between GLY molecules and surface functional groups of α-γ-Fe_2O_3-GO.

As shown previously, surface functional groups determined by FTIR were almost the same in all the composites. However, it is important to highlight that there are some differences between α-γ-Fe_2O_3-GO and $MnFe_2O_4$-rGO adsorption active sites, specifically in the type and the number of accessible adsorption sites. As proposed by the authors, electrostatic interaction is the principal mechanism of adsorption in these systems, and metallic centers are very important in this mechanism. They are Lewis acids, since they can act as electron-pair acceptors, while oxygenated charged groups of GLY are Lewis bases, because they are electron-pair donors. In addition, according to Pearson's acid–base theory, acids and bases could also be classified as hard and soft, depending on their size, charge, and polarizability. In addition, this theory states that soft acids prefer to react with soft bases and vice versa. In this case, oxygenated groups of GLY are hard bases, so they react preferably with hard acids. α-γ-Fe_2O_3-GO contains just Fe^{3+} metallic centers, while $MnFe_2O_4$-rGO contains Mn^{2+} and Fe^{3+} metallic centers, both being hard acids. Nevertheless, as Mn^{2+} radius is bigger than Fe^{3+} and they are isoelectronic, Mn^{2+} is softer than Fe^{3+}.

Another important difference is related to their crystal structures and particle morphology, and their relationship with the surface chemistry of exposed crystal facets on the iron minerals. Probably, the crystal structure of manganese ferrite impedes the optimal interaction between GLY and its metallic centers, while the crystal structures of hematite and maghemite possibly favor GLY adsorption because of the distribution of surface functional groups on a specific crystal face, which are considered as facet–dependent properties.

Other types of non-magnetic GBM have been synthesized, such as MOF composite, aerogel, and polymeric membrane. A composite of GO and a Zr-based MOF (known as UiO-67) were synthesized using a solvothermal methodology (Yang et al., 2017). The material labeled as UiO-67/GO presents a morphology in which MOF particles are densely dispersed on the surface of GO, with a mean particle size of 40 nm. On the other hand, graphene aerogel was synthesized (Ding et al., 2018) using ultrasonication treatment, in which a suspension of carboxymethyl chitosan was added dropwise into a GO suspension and PVA solution. The obtained product of this reaction was freeze-dried and labeled as CM-C/GA,

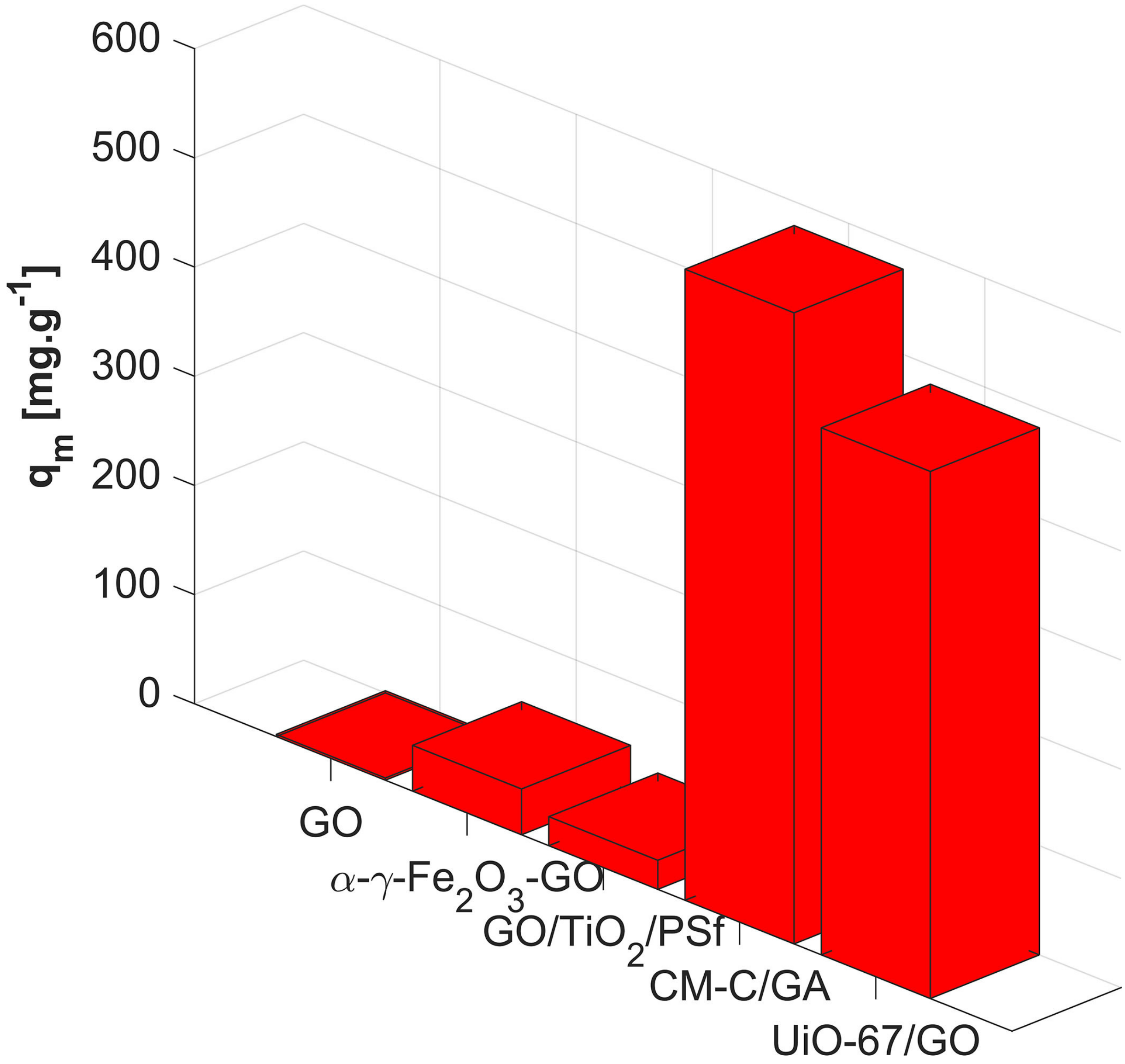

FIGURE 3
Langmuir's maximum adsorption capacity of GLY (Q_m) of GO (Santos et al., 2019), magnetic GO (Santos et al., 2019), and non-magnetic GBM (Yang et al., 2017; Ding et al., 2018; Hosseini and Toosi, 2019).

and it is characterized by having a heterogeneous porous structure conforming to a three–dimensional network typical of a foam. Finally, a GO/TiO_2 composite was prepared by solvothermal method and blended with polysulfone to obtain a membrane labeled as GO/TiO_2/PSf (Hosseini and Toosi, 2019). This membrane exhibits a sponge-like structure with interconnected voids.

Figure 3 presents Langmuir's maximum adsorption capacity of GLY (q_m) obtained at 25°C for pristine GO, magnetic α-γ-Fe_2O_3-GO, and non-magnetic GBM (GO/TiO_2/GO, CM-C/GA, and UiO-67/GO). As evidenced, the graphene aerogel and the MOF-GO composite present an exceptional adsorption capacity (578 and 482 $mg.g^{-1}$, respectively) compared to the other studied adsorbents. In contrast, the magnetic composite of best GLY adsorption performance (α-γ-Fe_2O_3-GO) has an adsorption maximum capacity that is more than 10 times lower than that of CM-C/GA and UiO-67/GO.

To compare the q_m value of each composite appropriately, it is necessary to consider the experimental conditions. In the case of CM-C/GA, the authors used the adsorbent dosage of 0.05 g L^{-1}, while in the experiments with UiO-67/GO, the adsorbent dosage was 0.1 g L^{-1}. These dosages are very small compared to those used in the experiments with magnetic composites (1 g L^{-1}). Adsorbent dosage is a very important factor that must be studied to optimize adsorption systems, because it influences the maximum adsorption capacity, adsorption removal percentage, and economic spending.

Surface functional groups of CM-C/GA are the same as GO, including an amide group that comes from the carboxymethyl chitosan structure. In the case of UiO-67/GO, it presents Zr–OH groups that favor the formation of complexes with phosphonic and carboxylic groups of GLY. The textural properties of UiO-67/GO were not characterized; however, as MOFs got a tunable pore structure with different types of cavities, it is well-documented that they develop high BET-specific surface areas ($>$1,000 m^2 g^{-1}) (Kaur et al., 2019), and hence it is necessary to determine these properties because it is a composite material. On the other hand, the pore structure of CM-C/GA was classified as a mesoporous material with an average pore diameter of 5.1 nm and a surface area of 507 m^2 g^{-1}.

In this case, the exceptional performance of CM-C/GA could be attributed principally to its high specific surface area and its porous network structure. According to the authors, the adsorption and removal of GLY using CM-C/GA are done *via* strong hydrogen bond interaction; however, it is important to say that pore filling is another mechanism that is probably present, considering its special textural and structural characteristics.

Even though there are some proposed adsorption mechanisms of GLY over GBM, there is still a lack of understanding of this mechanism. In addition, experimental studies on GLY–GBM interactions are limited, and therefore computational investigations have been conducted to explore these types of interactions at an atomic scale. Density functional theory (DFT) research has been performed to study the adsorption of GLY over GBM. In general terms, optimization of the electronic structures of isolated GLY and GBM are done, thus obtaining an energetic quantity for each one of the structures, i.e., E_{GLY} and E_{GBM}, respectively. Then the adsorption system GLY+GBM is optimized to obtain the total minimum energy of the system, E_{Total}. Finally, adsorption energy (E_{ads}) is calculated as the difference between the total energy and the energy of the isolated GLY and GBM structures ($E_{ads} = E_{Total} - E_{GLY} - E_{GBM}$).

An investigation was performed with pyridine-like nitrogen-doped graphene decorated with platinum and copper clusters (PNG/Pt-Cu) system (Gulati and Kakkar, 2020). In this case, they studied the effect of bimetallic cluster stoichiometry of $Pt_{4-n}Cu_n$ (n = 0–4) on the adsorption energy of GLY. The adsorption energy of GLY over PNG (with no metallic clusters) was calculated to be$-$0.31 eV, which shows that physisorption takes place in this system. This was also corroborated by the bond lengths and the absence of changes in the structural parameters of GLY and PNG (no reaction between them). Conversely, in PNG/Pt-Cu adsorption system, they found that the presence of bimetallic clusters enhances the reactivity toward GLY adsorption. Indeed, the PNG/Pt_3-Cu_1 was the adsorbent that presents the most favorable adsorption of GLY, with a calculated E_{ads} value of $-$1.58 eV, which means a chemisorption process, because both metals are involved in bond formation with GLY.

Another computational investigation was done to explore the adsorption mechanism of GLY on pristine G and G doped with Ti, V, Cr, B, Ca, N, Cu, O, Pt, and Pd (Li et al., 2021). They studied the feasibility of the formation of the G doped with these 10 atoms, optimizing each one of the systems and determining a formation energy $E_{formation}$. With these calculations, they concluded that Ca, O, and Pd are the most favorable dopants in comparison to the other seven. For the adsorption systems, they obtained an E_{ads} of $-$0.46 eV for the pristine G system, with the amino moiety (-NH) of GLY involved in adsorption, which shows a very weak interaction between GLY and G. On the other hand, the G doping enhanced GLY adsorption by improving E_{ads} (i.e., more negative). However, G doped with Ti, V, Cr, and B showed the most favorable interaction with GLY, among the other dopants, since the phosphonate group of GLY is the most active in this process. At this point, it is very important to highlight that it is not necessary that the dopants that interact very strongly with GLY are suitable candidates for GLY adsorption, because a very strong interaction could result in the remotion of the dopant from the G surface. Therefore, the authors concluded that Ca, O, and P are appropriate dopants of G to carry out GLY adsorption, because they not only enhanced GLY interaction but also formed the most stable doped G.

Perspectives and future works

The thermal techniques presented here allow to obtain GBM avoiding the use of other toxic techniques, such as Hummer's method. For this reason, these techniques result in greener synthesis methods in comparison to the traditional ones.

As to GLY adsorption using GBM, we showed that efficient and optimal adsorption systems have been designed, such as the G aerogel (CM-C/GA) and MOF-GO composite (UiO-67/GO). However, it is still necessary to investigate the application of these materials in dynamic adsorption, because this process mode is more used on a big scale. Also, it would be interesting to make an economic analysis comparing other carbonaceous materials with the same performance, because it is well-known that G is in principle an expensive material. In addition, as we propose here, graphene-derived materials obtained *via* the thermal treatment of biomass wastes could be used as precursors of already studied composites. So, it is necessary to investigate if similar, or the same, results are obtained when the graphite oxidation step (Hummers) is replaced with biomass pyrolysis under the conditions described above. If so, this represents an economic and environmental advantage during the synthesis of GBM.

Finally, computational investigations are a very important tool to understand the mechanism involved throughout the adsorption process. This favors the design of optimal adsorption systems because more focused experimental investigations could be carried out, reducing time and economic costs. Nevertheless, it is required to keep investigating the mechanisms to produce other GBM, such as GO, since this is the most common GBM used in the experimental investigations reported in the literature.

Author contributions

DH-B, VB, and LG collected the information and wrote the manuscript. DH-B made the figures. JM-P and PR-E revised and corrected the manuscript. All authors contributed to the article and approved the submitted version.

Funding

This work was funded by Science Faculty from Universidad de los Andes, with the project INV-509 2021-128-2257. An additional support of "Publica tus Nuevos Conocimientos y Expón tu Nuevas Creaciones", de la Vicerrectoría de investigaciones de la Universidad de los Andes (Bogotá, Colombia).

Acknowledgments

Authors want to thank 'Fondo de Apoyo Financiero para Doctorado' from Universidad de los Andes and Science Ministery from Colombia (MINCIENCIAS). The authors also thank the Research and Postgraduate Committee-Faculty of Sciences of the Universidad de los Andes, Colombia. On the other hand, the authors thank the framework agreement between Universidad Nacional de Colombia and Universidad de los Andes (Bogotá, Colombia) under which this work was carried out. Juan Carlos Moreno-Piraján also thank for an award from the Facultad de Ciencias of Universidad de los Andes, number INV-2021-128-2257.

Conflict of interest

The authors declare that the research was conducted in the absence of any commercial or financial relationships that could be construed as a potential conflict of interest.

Publisher's note

References

Aïssa, B., Memon, N. K., Ali, A., and Khraisheh, M. K. (2015). Recent progress in the growth and applications of graphene as a smart material: a review. *Front. Mater* 2, 58. doi: 10.3389/fmats.2015.00058

Al-Ghouti, M. A., and Da'ana, D. A. (2020). Guidelines for the use and interpretation of adsorption isotherm models: a review. *J. Hazard. Mater* 393, 122383. doi: 10.1016/j.jhazmat.2020.122383

Allen, M. J., Tung, V. C., and Kaner, R. B. (2010). Honeycomb carbon: a review of graphene. *Chem. Rev.* 110, 132–145. doi: 10.1021/CR900070D

Ambika, S., and Srilekha, V. (2021). Eco-safe chemicothermal conversion of industrial graphite waste to exfoliated graphene and evaluation as engineered adsorbent to remove toxic textile dyes. *Environ. Adv.* 4, 100072. doi: 10.1016/j.envadv.2021.100072

Antar, M., Lyu, D., Nazari, M., Shah, A., Zhou, X., and Smith, D. L. (2021). Biomass for a sustainable bioeconomy: An overview of world biomass production and utilization. *Renew. Sustain. Energy Rev.* 139, 110691. doi: 10.1016/j.rser.2020.110691

Banhart, F., Kotakoski, J., and Krasheninnikov, A. V. (2010). Structural defects in graphene. *ACS Nano* 5, 26–41. doi: 10.1021/nn102598m

Ding, C., Wang, X., Liu, H., Li, Y., Sun, Y., Lin, Y., et al. (2018). Glyphosate removal from water by functional three-dimensional graphene aerogels. *Environ. Chem.* 15, 325–335. doi: 10.1071/EN18087

Ding, K., Wang, Y., Liu, S., Lin, G., Syed-Hassan, S. S. A., Li, B., et al. (2021). Volatile-char interactions during biomass pyrolysis: insight into the activity of chars derived from three major components. *J. Anal. Appl. Pyrolysis* 159, 105320. doi: 10.1016/j.jaap.2021.105320

Dorontić, S., Jovanovi,ć, S., and Bonasera, A. (2021). Shedding light on graphene quantum dots: Key synthetic strategies, characterization tools, and cutting-edge applications. *Materials* 14, 6153. doi: 10.3390/ma14206153

Gulati, A., and Kakkar, R. (2020). DFT study of adsorption of glyphosate pesticide on Pt-Cu decorated pyridine-like nitrogen-doped graphene. *J. Nanoparticle Res.* 22, 1–15. doi: 10.1007/s11051-019-4730-z

Hong, W., Wang, X., Zheng, H., Li, R., Wu, R., and Chen, J. S. (2021). Molten-salt-assisted synthesis of nitrogen-doped carbon nanosheets derived from biomass waste of gingko shells as efficient catalyst for oxygen reduction reaction. *Processes* 9, 2124. doi: 10.3390/pr9122124

Hosseini, N., and Toosi, M. R. (2019). Removal of 2,4-D, glyphosate, trifluralin, and butachlor herbicides from water by polysulfone membranes mixed by graphene oxide/TiO2 nanocomposite: study of filtration and batch adsorption. *J. Environ. Heal. Sci. Eng.* 171, 247–258. doi: 10.1007/s40201-019-00344-3

Hou, J., Cao, C., Idrees, F., and Ma, X. (2015). Hierarchical porous nitrogen-doped carbon nanosheets derived from silk for ultrahigh-capacity battery anodes and supercapacitors. *ACS Nano* 9, 2556–2564. doi: 10.1021/nn506394r

International Agency for Research on Cancer (2015). "IARC monographs on the evaluation of carcinogenic risks to humans, volume 112," in *Some Organophosphate Insecticides and Herbicides.* Lyon: IARC. Available online at: https://publications.iarc.fr/549

Jiao, L., Wang, X., Diankov, G., Wang, H., and Dai, H. (2010). Facile synthesis of high-quality graphene nanoribbons. *Nat. Nanotechnol.* 5, 321–325. doi: 10.1038/nnano.2010.54

Jiao, L., Zhang, L., Wang, X., Diankov, G., and Dai, H. (2009). Narrow graphene nanoribbons from carbon nanotubes. *Nature* 458, 877–880. doi: 10.1038/NATURE07919

Kaur, G., Øien-ØDegaard, S., Lazzarini, A., Chavan, S. M., Bordiga, S., Lillerud, K. P., et al. (2019). Controlling the synthesis of metal-organic framework UiO-67 by tuning its kinetic driving force. *Cryst. Growth Des.* 19, 4246–4251. doi: 10.1021/acs.cgd.9b00916

Khalil, K. M. S., Allam, O. A. S., Khairy, M., Mohammed, K. M. H., Elkhatib, R. M., and Hamed, M. A. (2017). High surface area nanostructured activated carbons derived from sustainable sorghum stalk. *J. Mol. Liq.* 247, 386–396. doi: 10.1016/j.molliq.2017.09.090

Kong, X., Zhu, Y., Lei, H., Wang, C., Zhao, Y., Huo, E., et al. (2020). Synthesis of graphene-like carbon from biomass pyrolysis and its applications. *Chem. Eng. J.* 399, 125808. doi: 10.1016/j.cej.2020.125808

Kosynkin, D. V., Higginbotham, A. L., Sinitskii, A., Lomeda, J. R., Dimiev, A., Price, B. K., et al. (2009). Longitudinal unzipping of carbon nanotubes to form graphene nanoribbons. *Nature* 458, 872–876. doi: 10.1038/nature07872

Kulyk, B., Freitas, M. A., Santos, N. F., Mohseni, F., Carvalho, A. F., Yasakau, K., et al. (2022). A critical review on the production and application of graphene and graphene-based materials in anti-corrosion coatings. *Crit. Rev. Solid State Mater. Sci.* 47, 309–355. doi: 10.1080/10408436.2021.1886046

Kumar, N., Salehiyan, R., Chauke, V., Joseph Botlhoko, O., Setshedi, K., Scriba, M., et al. (2021). Top-down synthesis of graphene: a comprehensive review. *FlatChem* 27, 100224. doi: 10.1016/j.flatc.2021.100224

Li, G., Yoon, K. Y., Zhong, X., Zhu, X., and Dong, G. (2016). Efficient Bottom-Up Preparation of Graphene Nanoribbons by Mild Suzuki–Miyaura Polymerization of Simple Triaryl Monomers. *Chem. – A Eur. J.* 22, 9116–9120. doi: 10.1002/chem.201602007

Li, X., Yao, Y., Liu, J., and Zou, Z. (2017). Highly microporous nitrogen doped graphene-like carbon material as an efficient fuel cell catalyst. *Int. J. Hydrogen Energy* 42, 19903–19912doi: 10.1016/j.ijhydene.2017.06.017

Li, X., Zhang, R., Dong, F., Tang, Y., Xu, L., Sun, C., et al. (2021). Exploring adsorption mechanism of glyphosate on pristine and elemental doped graphene. *Chem. Phys. Lett.* 779, 138849. doi: 10.1016/j.cplett.2021.138849

Li, Y., Zhao, C., Wen, Y., Wang, Y., and Yang, Y. (2018). Adsorption performance and mechanism of magnetic reduced graphene oxide in glyphosate contaminated water. *Environ. Sci. Pollut. Res.* 25, 21036–21048. doi: 10.1007/s11356-018-2282-x

Ling, Z., Wang, Z., Zhang, M., Yu, C., Wang, G., Dong, Y., et al. (2016). Sustainable synthesis and assembly of biomass-derived B/N Co-doped carbon nanosheets with ultrahigh aspect ratio for high-performance supercapacitors. *Adv. Funct. Mater.* 26, 111–119. doi: 10.1002/adfm.201504004

Liu, K., Chen, B., Feng, A., Wu, J., Hu, X., Zhou, J., et al. (2022). Bio-composite nanoarchitectonics for graphene tofu as useful source material for capacitive deionization. *Desalination* 526, 115461. doi: 10.1016/j.desal.2021.115461

Liu, L., Qing, M., Wang, Y., and Chen, S. (2015). Defects in graphene: generation, healing, and their effects on the properties of graphene: a review. *J. Mater. Sci. Technol.* 31, 599–606. doi: 10.1016/j.jmst.2014.11.019

Liu, X., Giordano, C., and Antonietti, M. (2014). A facile molten-salt route to graphene synthesis. *Small* 10, 193–200. doi: 10.1002/smll.201300812

Ma, Z., Xing, X., Qu, Z., Sun, Y., Sun, G., Wang, X., et al. (2020). Activity of microporous lignin-derived carbon-based solid catalysts used in biodiesel production. *Int. J. Biol. Macromol.* 164, 1840–1846. doi: 10.1016/j.ijbiomac.2020.08.002

Marin, P., Bergamasco, R., Módenes, A. N., Paraiso, P. R., and Hamoudi, S. (2019). Synthesis and characterization of graphene oxide functionalized with MnFe2O4 and supported on activated carbon for glyphosate adsorption in fixed bed column. *Process Saf. Environ. Prot.* 123, 59–71. doi: 10.1016/j.psep.2018.12.027

Meftaul, I. M., Venkateswarlu, K., Dharmarajan, R., Annamalai, P., Asaduzzaman, M., Parven, A., et al. (2020). Controversies over human health and ecological impacts of glyphosate: is it to be banned in modern agriculture? *Environ. Pollut.* 263, 114372. doi: 10.1016/j.envpol.2020.114372

Mokoloko, L. L., Matsoso, B. J., Forbes, R. P., Barrett, D. H., Moreno, B. D., and Coville, N. J. (2021). Evolution of large-area reduced graphene oxide nanosheets from carbon dots via thermal treatment. *Carbon Trends* 4, 100074. doi: 10.1016/J.CARTRE.2021.100074

Nanaji, K., Sarada, B. V., Varadaraju, U. V., N., Rao, T., and Anandan, S. (2021). A novel approach to synthesize porous graphene sheets by exploring KOH as pore inducing agent as well as a catalyst for supercapacitors with ultra-fast rate capability. *Renew. Energy* 172, 502–513. doi: 10.1016/j.renene.2021.03.039

Novoselov, K. S., Geim, A. K., Morozov, S. V., Jiang, D., Zhang, Y., Dubonos, S. V., et al. (2004). Electric field in atomically thin carbon films. *Science* 306, 666–669. doi: 10.1126/SCIENCE.1102896

Park, S., and Ruoff, R. S. (2009). Chemical methods for the production of graphenes. *Nat. Nanotechnol.* 4, 217–224. doi: 10.1038/nnano.2009.58

Perondi, D., Bassanesi, G. R., Manera, C., Lazzari, L. K., Godinho, M., Zattera, A. J., et al. (2021). From cellulose to graphene-like porous carbon nanosheets. *Microporous Mesoporous Mater.* 323, 111217 doi: 10.1016/j.micromeso.2021.111217

Purkait, T., Singh, G., Singh, M., Kumar, D., and Dey, R. S. (2017). Large area few-layer graphene with scalable preparation from waste biomass for high-performance supercapacitor. *Sci. Rep.* 7, 1–14. doi: 10.1038/s41598-017-15463-w

Rajesh, A., Mangamma, G., Sairam, T. N., and Subramanian, S. (2019). Probing host-guest interactions in hydroxyapatite intercalated graphene oxide nanocomposite: NMR and scanning probe microscopy studies. *Chem. Phys. Lett.* 732, 136636. doi: 10.1016/J.CPLETT.2019.136636

Reina, A., Jia, X., Ho, J., Nezich, D., Son, H., Bulovic, V., et al. (2009). Large area, few-layer graphene films on arbitrary substrates by chemical vapor deposition. *Nano Lett.* 9, 30–35. doi: 10.1021/NL801827V

Rouquerol, F., Rouquerol, J., Sing, K. S. W., Maurin, G., and Llewellyn, P. (2014). *Introduction. Adsorpt by Powders Porous Solids Princ.* Cambridge, MA: Academic Press

Ruiz-Hitzky, E., Darder, M., Fernandes, F. M., Zatile, E., Palomares, F. J., and Aranda, P. (2011). Supported graphene from natural resources: easy preparation and applications. *Adv. Mater.* 23, 5250–5255. doi: 10.1002/adma.201101988

Saeed, M., Alshammari, Y., Majeed, S. A., and Al-Nasrallah, E. (2020). Chemical vapour deposition of graphene—synthesis, characterisation, and applications: a review. *Molecules* 25, 3856. doi: 10.3390/molecules25173856

Santos, T. R. T., Andrade, M. B., Silva, M. F., Bergamasco, R., and Hamoudi, S. (2019). Development of α- and γ-Fe_2O_3 decorated graphene oxides for glyphosate removal from water. *Environ. Technol.* 40, 1118–1137. doi: 10.1080/09593330.2017.1411397

Sillanpä, M., and Ncibi, C. (2019). "Getting hold of the circular economy concept," in *The Circular Economy* (Amsterdam: Elsevier), 1–35.

Sun, L., Tian, C., Li, M., Meng, X., Wang, L., Wang, R., et al. (2013). From coconut shell to porous graphene-like nanosheets for high-power supercapacitors. *J. Mater. Chem. A* 1, 6462–6470. doi: 10.1039/c3ta10897j

Tang, L., Ji, R., Li, X., Teng, K. S., and Lau, S. P. (2013). Size-dependent structural and optical characteristics of glucose-derived graphene quantum dots. *Part. Part. Syst. Charact.* 30, 523–531. doi: 10.1002/ppsc.201200131

Ueda Yamaguchi, N., Bergamasco, R., and Hamoudi, S. (2016). Magnetic $MnFe_2O_4$-graphene hybrid composite for efficient removal of glyphosate from water. *Chem. Eng. J.* 295, 391–402. doi: 10.1016/j.cej.2016.03.051

Viculis, L. H., Mack, J. J., and Kaner, R. B. (2003). A chemical route to carbon nanoscrolls. *Science* 299:1361. doi: 10.1126/SCIENCE.1078842

Wang, J., Ding, B., Hao, X., Xu, Y., Wang, Y., Shen, L., et al. (2016). A modified molten-salt method to prepare graphene electrode with high capacitance and low self-discharge rate. *Carbon* 102, 255–261. doi: 10.1016/j.carbon.2016.02.047

Xin, G., Hwang, W., Kim, N., Cho, S. M., and Chae, H. (2010). A graphene sheet exfoliated with microwave irradiation and interlinked by carbon nanotubes for high-performance transparent flexible electrodes. *Nanotechnology* 21. doi: 10.1088/0957-4484/21/40/405201

Yang, Q., Wang, J., Zhang, W., Liu, F., Yue, X., Liu, Y., et al. (2017). Interface engineering of metal organic framework on graphene oxide with enhanced adsorption capacity for organophosphorus pesticide. *Chem. Eng. J.* 313, 19–26. doi: 10.1016/j.cej.2016.12.041